



Repositorio Institucional de la Universidad Autónoma de Madrid

<https://repositorio.uam.es>

Esta es la **versión de autor** del artículo publicado en:

This is an **author produced version** of a paper published in:

Journal of the American Chemical Society 142.7 (2020): 3540-3547

DOI: <https://doi.org/10.1021/jacs.9b12389>

Copyright: © 2020 American Chemical Society

El acceso a la versión del editor puede requerir la suscripción del recurso

Access to the published version may require subscription

Biomimetic synthesis of sub-20 nanometer Covalent Organic Frameworks in water

Authors

Carlos Franco^{1†}, David Rodríguez-San-Miguel^{2†}, Alessandro Sorrenti¹, Semih Sevim¹, Ramon Pons³, Ana E. Platero-Prats², Marko Pavlovic^{4,5}, Istvan Szilágyi^{4,6}, M. Luisa Ruiz Gonzalez⁷, José M. González-Calbet⁷, Davide Bochicchio⁸, Luca Pesce⁸, Giovanni M. Pavan^{8,9}, Inhar Imaz¹⁰, Mary Cano-Sarabia¹⁰, Daniel MasPOCH^{10,11}, Salvador Pané¹², Andrew J. deMello¹, Felix Zamora^{2*}, Josep Puigmartí-Luis^{1*}

Affiliations

¹Department of Chemistry and Applied Biosciences, Institute for Chemical and Bioengineering, ETH Zurich, Vladimir Prelog Weg 1, 8093 Zurich, Switzerland.

²Departamento de Química Inorgánica, Institute for Advanced Research in Chemical Sciences (IAdChem) and Condensed Matter Physics Institute (IFIMAC). Universidad Autónoma de Madrid, 28049 Madrid, Spain.

³Institute for Advanced Chemistry of Catalonia (IQAC-CSIC), Jordi Girona 18-26, E-08034 Barcelona, Spain.

⁴MTA-SZTE Lendület Biocolloids Research Group, University of Szeged, H-6720 Szeged, Hungary.

⁵Max-Planck Institute of Colloids and Interfaces; Department of Colloid Chemistry, Am Mühlenberg 1, 14476 Potsdam, Germany

⁶Interdisciplinary Excellence Center, Department of Physical Chemistry and Materials Science, University of Szeged, H-6720 Szeged, Hungary.

⁷Departamento de Química Inorgánica, Universidad Complutense de Madrid, 28040 Madrid, Spain.

⁸Department of Innovative Technologies, University of Applied Sciences and Arts of Southern Switzerland, Galleria 2, Via Cantonale 2c, CH-6928 Manno, Switzerland.

⁹Department of Applied Science and Technology, Politecnico di Torino, Corso Duca degli Abruzzi 24, 10129 Torino, Italy.

¹⁰Catalan Institute of Nanoscience and Nanotechnology (ICN2), CSIC and BIST Campus UAB, Bellaterra, 08193 Barcelona, Spain.

¹¹ICREA, Pg. Lluís Companys 23, 08010 Barcelona, Spain.

¹²Multi-Scale Robotics Lab ETH Zurich Tannenstrasse 3, CH-8092 Zurich, Switzerland.

Abstract

Covalent organic frameworks (COFs) are commonly synthesized under harsh conditions yielding unprocessable powders. Control in their crystallization process and growth has been limited to studies conducted in hazardous organic solvents. Herein, we report a one-pot synthetic method that yields stable aqueous colloidal solutions of sub-20 nm crystalline imine-based COF particles at room temperature and ambient pressure. Additionally, through the combination of experimental and computational studies, we investigated the mechanisms and forces underlying the formation of such imine-based COF colloids in water. Further, we show that our method can be used to process the colloidal solution into 2D and 3D COF shapes, as well as to generate a COF ink that can be directly printed onto surfaces. These findings should open new vistas in COF chemistry enabling new application areas.

Introduction

Covalent organic frameworks (COFs) are porous crystalline materials generated from organic molecules linked via reversible covalent bonds.¹ Since its discovery, COF chemistry has facilitated a modular construction of periodic crystalline matter by connecting molecular subunits in a predictable and modular fashion.² This strategy has proved efficient in generating extended crystalline and porous networks possessing permanent porosity, high specific surface areas and excellent thermal/chemical stability; features that have found potential applications in a vast number of fields.³ However, conventional routes for COF synthesis involve high temperatures, which when combined with the low solubility of the initial building blocks in common reaction media, yield poor control over the size of the crystalline domains and the morphology of COF crystals.⁴ Unsurprisingly, such drawbacks have hampered the extraction of reliable information regarding the effects of crystallite size and morphology on COF properties. Accordingly, much

effort is now focused on both understanding and controlling the growth of COF crystals at length scales spanning the nanometer to micron scales.

Recently, Dichtel and co-workers reported on the preparation of stable particles of boronate ester-linked COFs, whose size can be modulated between 40 and hundreds of nanometers by using mixtures of organic solvents at high temperature.⁵ Later, such COFs colloidal solutions in organic media have been used by the same authors for preparing micron-sized single crystals of boronate ester-linked COFs via a seeded growth procedure.⁶ Therefore, having access to nanometer-sized particles of COFs allowed the authors to overcome a long-standing challenge in the field, i.e. the formation of large single crystals of COFs. Besides this specific example, COF crystal-downsizing will be key to transforming COFs from unprocessable crystalline powders into processable materials, integrating COFs into nanoscale devices,⁷ as well as establishing relationships between COF crystal size and properties. In addition, COF crystal downsizing will expand the range of applications of these materials, such as in the biomedical, device and printing arenas,⁸ and enhance their bioavailability.⁹ However, only nanoparticles of boronate ester-linked COFs in organic solvents have been reported so far.⁵ Unfortunately, boron-based COFs have poor chemical stabilities, which limits their practical implementation. In addition, the fact that hazardous organic solvents are still required as a medium to stabilize their colloidal dispersion precludes their use in biological environments. In contrast, imine-based COFs are significantly more stable and robust for practical use.¹⁰ Nevertheless, despite the high number of reports on imine-based COFs, it has not been possible yet to downsize them to the nanoscale.¹¹ Put simply, routes for producing aqueous colloidal solutions of imine-linked COF nanoparticles are still missing.

To overcome this limitation, we report here an efficient one-pot method to generate stable and homogeneous colloidal solutions of sub-20 nanometer imine-linked COF particles in water. The synthesis of crystalline COF colloids was performed for the first time at room temperature using micelles as reaction nanocompartments. This approach was inspired by living systems that make use of confined volumes (such as intracellular compartments) to control crystallization processes in aqueous media.^{12–16} This method allowed us to use a combination of experimental scattering techniques in solution, that together with computational calculations, gave unprecedented insights into the mechanism and forces underlying the formation of imine-linked COFs. Additionally, we show that the produced colloids enable the processing of COFs into 2D and 3D shapes such as crystalline freestanding films and monoliths. Further, we prove that such colloids can also be used as inks to directly print COFs onto surfaces. Finally, we demonstrated the generality of our method by applying it to the synthesis of metal-organic frameworks (MOFs) colloids. In particular, we show the synthesis of 20 nanometer MIL-100(Fe) particles at room temperature and ambient pressure. MIL-100(Fe) is a prototypical MOF that requires harsh conditions for its synthesis¹⁷ and only forms larger crystals.¹⁸ We expect that the presented methodology will vastly increase knowledge on structure-property correlations in COFs and MOFs, allowing access to a large number of new applications and functions, whilst significantly enhancing the bioavailability and processability of these materials.

Results and Discussion

TAPB-BTCA COF is typically obtained via imine condensation between 1,3,5-tris(4-aminophenyl)benzene (**TAPB**) and 1,3,5-triformylbenzene (**BTCA**) in *meta*-cresol or DMSO. Additionally, acetic acid is used as a catalyst to yield **TAPB-BTCA COF** as an insoluble and unprocessable crystalline powder.¹⁹ Herein, we employed the *catanionic* micellar system^{20,21}

formed from a mixture of cationic hexadecyltrimethylammonium bromide (CTAB) and anionic sodium dodecyl sulfate (SDS) surfactants (CTAB/SDS 97:3) to generate stable colloidal solutions of crystalline **TAPB-BTCA COF** nanoparticles in water (**Fig. 1A**). Note that this surfactant ratio guarantees the formation of small mixed micelles in the *catanionic* mixture, instead of bigger vesicles as previously reported,²⁰ and here it was optimized to achieve the smallest size of colloiddally stable **TAPB-BTCA COF** nanoparticles (**Fig. S1**). The micellar medium allows the solubilization in water of the otherwise insoluble molecular building blocks **BTCA** and **TAPB** at room temperature, yielding two homogeneous solutions of the reactants loaded into CTAB/SDS mixed micelles.²² After mixing the solutions and adding acetic acid, the reaction mixture turned orange, indicating the formation of imine bonds characteristic of **TAPB-BTCA COF** growth. However, and in contrast to observations in standard synthetic protocols, the reaction mixture remained clear and homogeneous with no apparent precipitation (**Fig. 1B**), even after storage at room temperature for six months. Indeed, when irradiated with a laser ($\lambda = 630$ nm), the reaction mixture clearly exhibited Willis–Tyndall scattering behavior,²³ confirming the presence of colloidal particles (**Fig. S2**). To validate the existence of crystalline **TAPB-BTCA COF** nanoparticles in the reaction mixture, synchrotron X-ray diffraction measurements were performed directly on the colloidal solution generated after mixing. The experimental differential diffraction data were fitted using the Le Bail method^{24,25} against the reported structural model for **TAPB-BTCA COF** (*P3*, $a \sim 15.91$ Å and $c \sim 3.54$ Å as refined cell parameters) (**Fig. 1C**), demonstrating the presence of the crystalline COF phase with a main low-angle peak centered at $q = 0.46$ Å⁻¹ associated with the (100) Bragg reflection.¹⁹ Accordingly, this result unambiguously confirmed the formation of crystalline **TAPB-BTCA COF** nanoparticles via the mixed micelle method. The sizes and morphology of the obtained **TAPB-BTCA COF** nanoparticles were subsequently studied by dynamic light scattering (DLS) and cryogenic transmission electron

microscopy (cryo-TEM). DLS measurements conducted on the reaction mixture after 24 hours (**Fig. S3A**) reported a monodisperse distribution of scatterers centred at 16 nm. Remarkably, the colloidal behaviour of the reaction mixture remains stable and homogeneous (with no appreciable turbidity or size increase) for periods in excess of six months (**Fig. S3B**). Additionally, cryo-TEM images of the reaction mixture after 24 hours (**Fig. 1D**) showed two different populations of objects; one centred at 5 ± 1 nm and the other at 16 ± 1 nm in diameter. The former value correlated well with the size of surfactant micelles determined by small-angle X-ray scattering (SAXS) in the pure CTAB/SDS (97:3) mixture (see below and **Fig. S4**), with the latter comparing well with the size distribution measured by DLS, and thus being ascribed to **TAPB-BTCA COF** nanoparticles. The high-resolution transmission electron microscopy (HR-TEM) study of drop cast reaction mixtures further confirmed the crystallinity of **TAPB-BTCA COF** nanoparticles. **Fig. 1E** shows a characteristic HRTEM image and its corresponding Fast Fourier Transform (FFT). The measured periodicities (white arrows in **Fig. 1E**) match well with the unit cell geometry of **TAPB-BTCA COF** as viewed along the $[-211]$ zone axis. **Fig. 1F** presents a magnified detail of the above HR-TEM image overlapped with the simulated crystal structure of **TAPB-BTCA COF** viewed along the $[-211]$ zone axis, suggesting a good match between the light and dark fringes of the micrograph and the higher and lower atomic density regions of the COF structure. Additionally, scanning electron microscopy (SEM) images of drop cast reaction mixtures revealed the presence of well-defined and uniform nanoparticles (and nanoparticle clusters), with a size that correlates well with both DLS and cryo-TEM measurements (**Fig. S1A**).

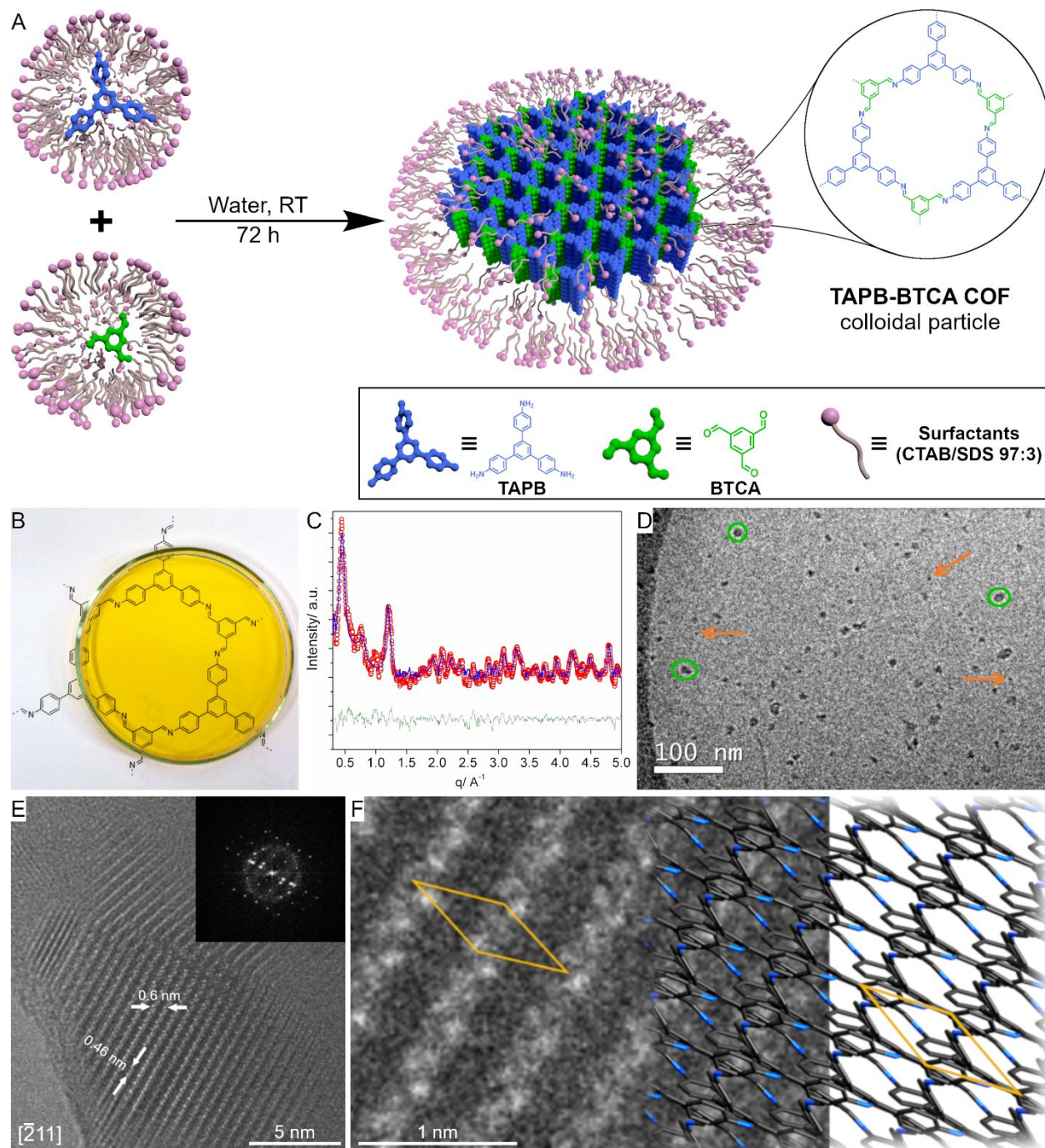


Fig. 1. TAPB-BTCA COF nanoparticles. (A) Schematic representation of the synthesis of colloidal **TAPB-BTCA COF** nanoparticles in water. (B) Photograph of the transparent reaction mixture. (C) Synchrotron X-ray differential diffraction data of the reaction mixture containing **TAPB-BTCA COF** nanoparticles. Experimental differential data obtained after subtracting the data corresponding to the solvent mixture to that collected on reaction mixture containing **TAPB-BTCA COF** nanoparticles are shown in red, with the calculated fit using $P3$, $a \sim 15.91 \text{ \AA}$ and $c \sim 3.54 \text{ \AA}$ as refined cell parameters in blue and associated residuals in green with R_p and R_{wp} values of 16.3 % and 13.7

%, respectively. **(D)** Cryo-TEM image of **TAPB-BTCA COF** colloid. For clarity, some **TAPB-BTCA COF** nanoparticles are outlined in green and some micelles are indicated by orange arrows. **(E)** HR-TEM image of a **TAPB-BTCA COF** nanoparticle along the $[-211]$ zone axis, with the inset showing the FFT. **(F)** Magnified HR-TEM image of a defined area in **(E)** overlaid with the schematic structural model of **TAPB-BTCA COF** along the $[-211]$ projection.

After confirming that sub-20 nanometer **TAPB-BTCA COF** particles can be generated, we investigated the possibility of isolating the COF material as a bulk solid. To this purpose, we added ethanol to the reaction mixture to destabilize the surfactant aggregates,²⁶ which triggered the flocculation of **TAPB-BTCA COF** nanoparticles as an insoluble yellow powder, hereafter termed **TAPB-BTCA COF(s)**. After flocculation, **TAPB-BTCA COF(s)** could be simply isolated from the reaction mixture by centrifugation. **TAPB-BTCA COF(s)** was characterized by Fourier-transform infrared (FT-IR) spectroscopy and solid-state Cross Polarization/Magic Angle Spinning Nuclear Magnetic Resonance (¹³C CP-MAS NMR). FT-IR spectra confirmed the presence of imine bonds through the appearance of the characteristic imine C=N stretching band at 1623 cm⁻¹ (**Fig. S5**), while solid state ¹³C CP-MAS NMR spectra exhibited the representative signal of the imine carbon atom at 157.1 ppm (**Fig. S6**). Additionally, powder X-ray diffraction (PXRD) patterns of **TAPB-BTCA COF(s)** (**Fig. S7**) were in excellent accordance with those previously reported for this material.¹⁹ It should be noted that the measured PXRD peaks were broader than those usually observed for **TAPB-BTCA COF(s)** prepared by conventional bulk synthetic methods,¹¹ suggesting the presence of smaller crystalline domains in **TAPB-BTCA COF(s)**.²⁷ The permanent porosity of **TAPB-BTCA COF(s)** was also confirmed by nitrogen adsorption isotherm measurements on previously activated samples, showing a characteristic isotherm with a Brunauer–Emmet–Teller (BET) area (A_{BET}) of 687 m² g⁻¹ at 77 K (**Fig. S8**). Finally, the CO₂ and water sorption properties of **TAPB-BTCA COF(s)** were also measured

(**Fig. S9** and **S10**). It was found to be porous to CO₂ with a total uptake of 9 mmol g⁻¹ at 203 K and 760 torr (1 mmol g⁻¹ at 298 K and 760 torr). Moreover, water-vapour sorption isotherms showed a step between 40-50% relative humidity, after which the water uptake increases monotonically until a maximum of 15% in mass (0.15 g_{water} g_{COF}⁻¹), which is the typical behaviour for this class of materials bearing hydrophobic walls.¹¹

To clarify the processes underlying the formation of **TAPB-BTCA COF** nanoparticles in the *catanionic* micellar medium, time-resolved *in-situ* DLS and SAXS experiments were performed. DLS indicated that the average hydrodynamic diameter of colloidal particles increased during the first few hours (after the addition of acetic acid), leveling off to yield a final average hydrodynamic diameter of 16 nm (**Fig. S11**). In contrast, when the synthesis was performed in pure CTAB micelles (*i.e.* without SDS), the size of **TAPB-BTCA COF** continued to increase until precipitation occurred. Accordingly, the role of the anionic surfactant was clearly evidenced, with SDS reducing the electrostatic repulsion of CTAB heads in the micellar aggregates (*i.e.* decreasing the surface energy), and favoring the formation of assemblies with lower curvatures.^{21,28} This is demonstrated by the increase in size of the nanoparticles when increasing the amount of SDS in the CTAB/SDS mixture (**Table S1**). In addition, the decrease in curvature caused by SDS facilitates the colloidal stabilization of COF oligomers and of the final **TAPB-BTCA COF** nanoparticles even over extended periods of time. Time-resolved SAXS experiments provided further insights into the growth mechanism of **TAPB-BTCA COF** nanoparticles. SAXS spectra of the two micellar solutions containing the **TAPB** and **BTCA** precursors (in the presence of acetic acid) indicated the existence of 4.8 ± 2 nm diameter ellipsoidal micelles; comparable to what it was observed in pure CTAB/SDS (97:3) solutions (**Fig. S4**). These data indicate that solubilization of COF precursors has a negligible effect on the

size and shape of the CTAB/SDS micellar aggregates. However, after mixing the two micellar solutions loaded with COF precursors, clear changes in the SAXS profiles were observed as a function of time. Scattering profiles at selected reaction times (5, 13, and 21 hours) are shown in **Fig. 2**, along with their best fits obtained from the used scattering model (further details are provided in Supplementary Materials). These three SAXS spectra describe three different regimes during the progress of the reaction (**Fig. 2A-C** and **Fig. S12**). At short reaction times (5 hours in **Fig. 2A**), SAXS profiles fit well to a disk-particle model with a radius of 6.4 nm and a thickness of 0.354 nm, which corresponds to a single layer of bare **TAPB-BTCA COF** (**Fig. S13A** and **Table S2**). As the reaction proceeded (13 hours in **Fig. 2B**), SAXS data showed a significant increase in intensity at low values of the scattering vector ($q < 1 \text{ nm}^{-1}$), together with the appearance of a broad feature around 2 nm^{-1} , suggesting changes of electron density contrast (further discussion on the particle models used for the analysis of the SAXS data, including details of the fitting procedure are provided in the Supplementary Materials).²⁹ This spectrum could then be better fitted to a COF-core@double-shell disk model, with a core thickness of 0.91 nm corresponding to a three-layered **TAPB-BTCA COF** stack surrounded by surfactant molecules (**Fig. S13B** and **Table S2**). At longer reaction times (21 hours in **Fig. 2C**), the SAXS profile showed a marked change at $q < 1 \text{ nm}^{-1}$, with a clear slope variation at 0.5 nm^{-1} . This spectrum could also be described using a COF-core@double-shell disk model, but with a core radius of 8.9 nm and a thickness of 3.74 nm (**Fig. S13B** and **Table S2**). This thickness corresponds to ten-layered **TAPB-BTCA COF** stacks fully covered by surfactant. Importantly, these extracted values were in good agreement with the overall size of the colloidal particles as measured by DLS and cryo-TEM. It should be noted that the formation of a compact surfactant layer around the COF nanoparticles is crucial for their stabilization in the reaction mixture, preventing further growth and flocculation. Accordingly, SAXS data suggest that after an initial

phase of lateral growth by covalent polymerization, the increase in size of **TAPB-BTCA COF** nanoparticles is essentially driven by the π - π stacking of COF layers (**Table S2**). Coarse grained molecular dynamics (CG-MD) simulations of single-, three- and ten-layered **TAPB-BTCA COF** particles were performed to gain further insight into the forces driving the self-assembly process. The simulations were run in water as well as hexadecane to simulate the hydrophobic environment of the micellar interior (see Supplementary Materials for further details about the CG model and simulations).

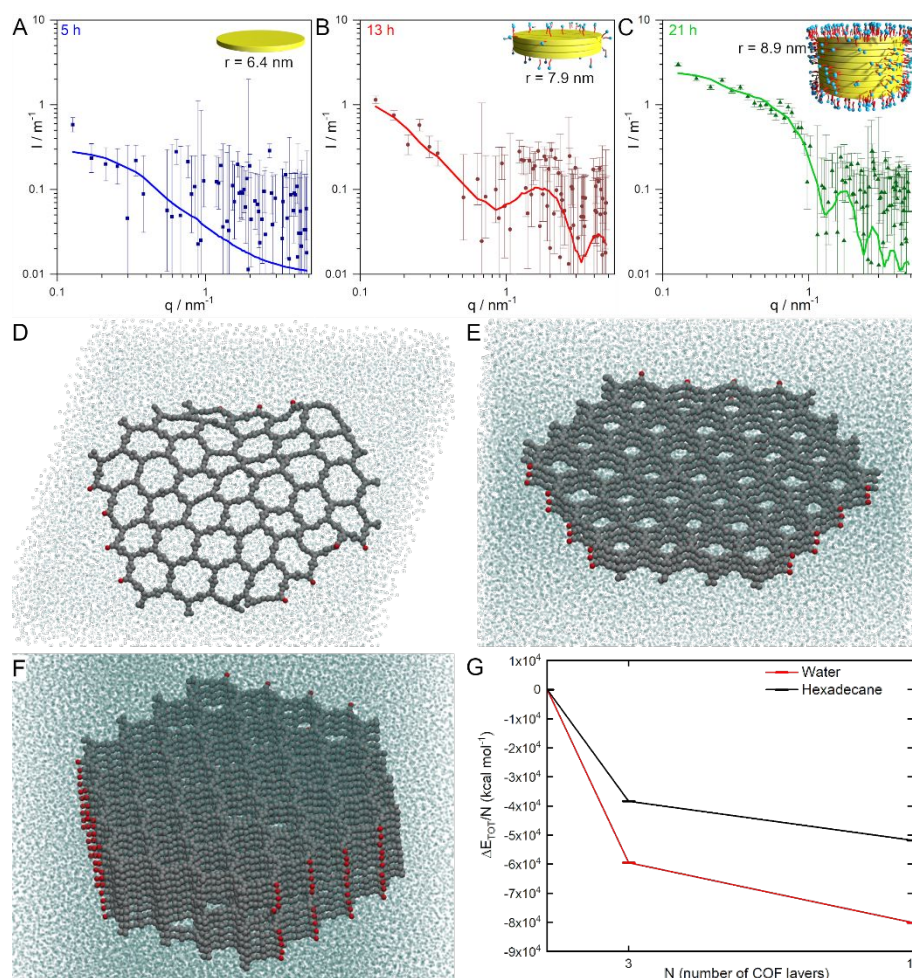


Fig. 2. Growth of TAPB-BTCA COF nanoparticles. (A), (B) and (C) SAXS spectra of the reaction mixture at 5, 13 and 21 hours, respectively. Experimental data (symbols) and best fits to the used scattering model (line). The insets illustrate the species measured at the three different regimes, with yellow disks representing the **TAPB-BTCA**

COF core, red cylinders the hydrophobic tails of the surfactants, and blue spheres their polar heads. (D), (E) and (F) Snapshots of TAPB-BTCA COF assemblies comprising 1, 3 and 10 layers respectively, after CG-MD simulation in water. (G) Total interaction energy (sum of solute-solute + solute-solvent + solvent-solvent interaction terms) between the COF layers normalized per-COF layer, $\Delta E_{\text{COF}/N}$, calculated from the MD simulations of TAPB-BTCA COF assemblies in water (red) and hexadecane (black). Energy of a single layer set to 0 as reference in the plot. The $\Delta E_{\text{COF}/N}$ becomes more and more favorable while the number of layers in the COF stacking increases, that is an evidence of cooperativity.

Fig. 2 D-F present snapshots of the equilibrated assemblies in water (see **Fig. S14** for the associated simulations in hexadecane). Simulations confirmed the strong cooperativity in the interaction between COF layers in both solvents, where the total interaction energy per-COF layer ($\Delta E_{\text{COF}/N}$: accounting for solute-solute + solute-solvent + solvent-solvent interactions) becomes more and more favorable for the three and ten-layered TAPB-BTCA COF particles. Comparing the two cases, the aggregation is found stronger and more cooperative in water than in hexadecane (**Fig. 2G**, total energetic gain per-COF layer), suggesting that the self-assembly and stacking of the COF layers is globally more stabilized in water (higher cooperativity) compared to hexadecane (lower cooperativity). However, when considering only the solute-solute contribution in this analysis, the data extracted from the simulations show that the cooperativity, although always present, is rather similar in the two cases (**Fig. S15**). Altogether, these results indicate that the additional driving force that makes the aggregation more cooperative in water than in hexadecane can be imputed to solvent effects. The more the COF layers interact between them, the less these interact with solvent molecules, which interact more between them. The fact that this leads to a greater advantage in water is consistent with the hydrophobic nature of the COF layers. In other words, the driving force for aggregation predominantly arises due to an increase in the water-water interactions upon COF aggregation,

that is a signature of the hydrophobic effect. In addition, MD simulations reveal a higher flexibility of the COF single-layer, which deformed significantly during the simulations (e.g. **Fig. 2D** and **Fig. S14**) compared to the stacked systems (**Fig. 2E-F**). These data also explain the greater tendency of surfactant molecules to interact with thicker assemblies (as measured by SAXS), since rigid COF stacks have more extended hydrophobic patches (e.g. pore walls) than rippled single-layers.

In addition to the importance of obtaining colloidal solutions of sub-20 nanometer COF particles in water, the described methodology also offers new opportunities for particle processing. Indeed, until now, a major limitation for the further implementation of COFs outside of laboratory environments has been their unprocessable nature.³⁰ Here, we show that by controlling the flocculation and aggregation of **TAPB-BTCA COF** nanoparticles in the reaction mixture (through the addition of ethanol), 2D and 3D **TAPB-BTCA COF** shapes could be easily achieved. For example, films of **TAPB-BTCA COF(s)** on the millimeter scale were prepared by confining a concentrated reaction mixture into a home-made microengineered clamp (**Fig. 3A**), followed by evaporation of the solvent. The concentrated reaction mixture was prepared by exchanging water for ethanol (further details are provided in the Supplementary Materials). We observed that highly uniform freestanding films with controlled thickness in the range of 0.5 to 50 μm were efficiently obtained via this approach (**Fig. 3B** and **Fig. S16-17**). Alternatively, reducing the size of the home-made microengineered clamp to squares of 500 μm lateral size or even changing its 2D shape to 3D morphologies led to the generation of smaller **TAPB-BTCA COF(s)** films (**Fig. S18**) or 3D octahedrons (**Fig. 3C** and Supplementary Materials). SEM analysis of these structures showed a nanoparticulated texture similar to the one observed for **TAPB-BTCA COF(s)** (**Fig. S19**). These data indicate that the processing steps allowed **TAPB-**

BTCA COF(s) to be shaped into 2D and 3D morphologies, with negligible reductions in the integrity of the COF material. Additionally, PXRD patterns of these structures were identical to those previously reported in the literature for this COF (**Fig. S20A**). Interestingly, the controlled diffusion of ethanol to the reaction mixture through a 3D flow-focusing microfluidic device allowed us to generate a processable COF ink from the initial colloidal solution. Indeed, the laminar flow conditions operating within such a device provided control over the flocculation and aggregation of **TAPB-BTCA COF** nanoparticles (**Fig. 3D**). Accordingly, a direct printing of **TAPB-BTCA COF(s)** onto surfaces was possible through the tubing connected to the outlet of the microfluidic device (**Fig. 3E** and **Video S1**). PXRD analysis of the printed structures confirmed that **TAPB-BTCA COF(s)** was deposited (**Fig. S20B**).

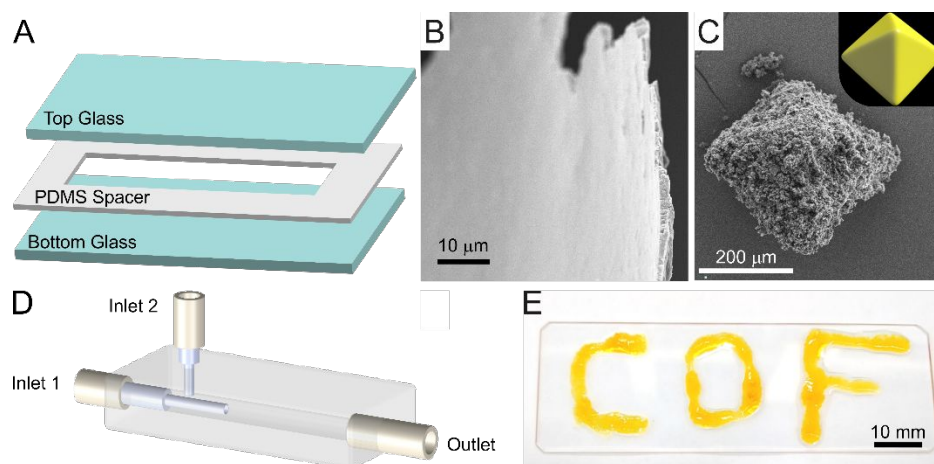


Fig. 3. Processability of the reaction mixture. (A) Schematic illustration of the home-made microengineered clamp used to generate **TAPB-BTCA COF(s)** films. (B) SEM image of the cross-section of a freestanding mm-sized film obtained using the setup shown in (A). (C) SEM image of a **TAPB-BTCA COF(s)** octahedron (500 μm edge). (D) Schematic illustration of the continuous 3D flow-focusing microfluidic device used to print **TAPB-BTCA COF(s)**. The reaction mixture was directly injected through inlet 1, while ethanol was introduced via inlet 2. (E) Photograph of "COF" printed with **TAPB-BTCA COF** on a planar surface using the device shown in (D).

To demonstrate the generality of our method, we prepared another imine-based COF, namely **Tz-COF**³¹ via the reaction of 2,4,6-tris(4-aminophenyl)-1,3,5-triazine and **BTCA** in a CTAB/SDS (97:3) mixture. SEM, DLS, and PXRD analysis clearly confirmed the formation of **Tz-COF** particles with a size distribution centered around 20 nm (**Fig. S21-S24**).³² Permanent porosity was measured using BET analysis, with results agreeing with previously reported values for the same COF material (**Fig. S25**).³³ Finally, it is significant to note that our method can be extended to MOFs. To demonstrate such generality, we synthesized a prototypical MOF that requires harsh conditions to crystalize, *i.e.* **MIL-100(Fe)**¹⁷. *In-situ* synchrotron X-ray diffraction measurements of the homogenous reaction mixture clearly confirmed the formation of **MIL-100(Fe)** (**Fig. S26**). Furthermore, DLS measurements of drop-cast reaction mixtures indicated a particle size distribution centered around 20 nm (**Fig. S27**). To the best of our knowledge, this is the smallest size reported for this biodegradable and non-toxic MOF.³⁴ After flocculation of the colloid with ethanol, PXRD and BET analysis of the resulting powder additionally confirmed the formation of **MIL-100(Fe)**, (**Fig. S28** and **Fig. S29**, respectively). Surprisingly, and in spite of the nanometer size of the generated **MIL-100(Fe)** particles, the measured BET surface area was high (1068 m²g⁻¹).

Conclusion

In summary, we have demonstrated a mild procedure for the preparation of stable aqueous colloidal solutions of crystalline imine-linked COF nanoparticles assisted by micelles of a *catanionic* surfactant mixture. The micellar medium provides control over the growth of the COF crystallites, which allowed us to reach the smallest size for COF particles among those reported so far. Additionally, by a combination of experimental and computational studies, we were able to shed light into the mechanism and forces underlying the growth of such COF

colloids. Note that this mechanistic study is unprecedented for imine-based COFs. Remarkably, the colloidal nature of the formed imine-based COF nanoparticles enabled their processing into 2D and 3D shapes, as well as the generation of an ink for their direct printing onto surfaces. Finally, to demonstrate the generality of our method we extended it to the preparation of colloidal nanoparticles of other porous crystalline materials, such as MOFs. We foresee that the preparation of chemically stable and easily processable imine-based COF colloids will open the door to new applications of these materials, for example in the field of functional devices, due to improved integration possibilities, or biomedicine, thanks to improved bioavailability.

ASSOCIATED CONTENT

Supporting Information: Materials and Methods; Supplementary Text; Figures S1-S33; Tables S1, S2; Movie S1.

Data and materials availability: All data needed to evaluate the conclusions in the article is present in the main text and supplementary materials.

AUTHOR INFORMATION

Corresponding Author: *Correspondence to: felix.zamora@uam.es, jpuigmarti@ethz.ch.

Author Contribution: † Carlos and David David Rodríguez-San-Miguel contributed equally to this work.

Competing financial interests: A patent related to the work presented in this document has been filed.

ACKNOWLEDGMENTS

This work was supported by the European Union (ERC-2015-STG microCrysFact 677020), the Swiss National Science Foundation (Project no. 200021_181988), ETH Zürich and Ministry of Science, Innovation and Universities MICINN (MAT2016-77608-C3-1P). R.P. acknowledges the Spanish MINECO (Grant No. CTQ2017—88948-P). A.E.P.P. acknowledges a TALENTO grant (2017-T1/IND5148) from Comunidad de Madrid. D.M. acknowledges financial support from the European Union (ERC-Co 615954). ICN2 is supported by the Severo Ochoa program from the Spanish MINECO (Grant No. SEV-2017-0706). We acknowledge DESY (Hamburg, Germany), a member of the Helmholtz Association HGF, for the provision of experimental facilities. Synchrotron X-ray diffraction experiments with COF-TAPB-BTCA were carried out at the beamline P02.1 PETRA III under the proposal I-20170717 EC. We acknowledge Jaume Caelles for SAXS/WAXS measurements performed at IQAC-CSIC.

REFERENCES

- (1) Côté, A. P.; Benin, A. I.; Ockwig, N. W.; O’Keeffe, M.; Matzger, A. J.; Yaghi, O. M. Porous, Crystalline, Covalent Organic Frameworks. *Science* **2005**, *310* (5751), 1166–1170. <https://doi.org/10.1126/science.1120411>.
- (2) Feng, X.; Ding, X.; Jiang, D. Covalent Organic Frameworks. *Chemical Society Reviews* **2012**, *41* (18), 6010–6022. <https://doi.org/10.1039/C2CS35157A>.
- (3) L. Segura, J.; J. Mancheño, M.; Zamora, F. Covalent Organic Frameworks Based on Schiff-Base Chemistry: Synthesis, Properties and Potential Applications. *Chemical Society Reviews* **2016**, *45* (20), 5635–5671. <https://doi.org/10.1039/C5CS00878F>.
- (4) Huang, N.; Wang, P.; Jiang, D. Covalent Organic Frameworks: A Materials Platform for Structural and Functional Designs. *Nature Reviews Materials* **2016**, *1* (10), 16068. <https://doi.org/10.1038/natrevmats.2016.68>.
- (5) Smith, B. J.; Parent, L. R.; Overholts, A. C.; Beaucage, P. A.; Bisbey, R. P.; Chavez, A. D.; Hwang, N.; Park, C.; Evans, A. M.; Gianneschi, N. C.; Dichtel, W. R. Colloidal Covalent Organic Frameworks. *ACS Cent. Sci.* **2017**, *3* (1), 58–65. <https://doi.org/10.1021/acscentsci.6b00331>.
- (6) Evans, A. M.; Parent, L. R.; Flanders, N. C.; Bisbey, R. P.; Vitaku, E.; Kirschner, M. S.; Schaller, R. D.; Chen, L. X.; Gianneschi, N. C.; Dichtel, W. R. Seeded Growth of Single-Crystal Two-Dimensional Covalent Organic Frameworks. *Science* **2018**, *361* (6397), 52–57. <https://doi.org/10.1126/science.aar7883>.
- (7) Wang, S.; McGuirk, C. M.; d’Aquino, A.; Mason, J. A.; Mirkin, C. A. Metal–Organic Framework Nanoparticles. *Advanced Materials* **2018**, *0* (0), 1800202. <https://doi.org/10.1002/adma.201800202>.
- (8) Sakata, Y.; Furukawa, S.; Kondo, M.; Hirai, K.; Horike, N.; Takashima, Y.; Uehara, H.; Louvain, N.; Meilikhov, M.; Tsuruoka, T.; Isoda, S.; Kosaka, W.; Sakata, O.; Kitagawa, S. Shape-Memory Nanopores Induced in Coordination Frameworks by Crystal Downsizing. *Science* **2013**, *339* (6116), 193–196. <https://doi.org/10.1126/science.1231451>.
- (9) Sindoro, M.; Yanai, N.; Jee, A.-Y.; Granick, S. Colloidal-Sized Metal–Organic Frameworks: Synthesis and Applications. *Accounts of Chemical Research* **2014**, *47* (2), 459–469. <https://doi.org/10.1021/ar400151n>.
- (10) DeBlase, C. R.; Dichtel, W. R. Moving Beyond Boron: The Emergence of New Linkage Chemistries in Covalent Organic Frameworks. *Macromolecules* **2016**, *49* (15), 5297–5305. <https://doi.org/10.1021/acs.macromol.6b00891>.
- (11) Rodríguez-San-Miguel, D.; Yazdi, A.; Guillerm, V.; Pérez-Carvajal, J.; Puentes, V.; MasPOCH, D.; Zamora, F. Confining Functional Nanoparticles into Colloidal Imine-Based COF Spheres by a Sequential Encapsulation–Crystallization Method. *Chemistry – A European Journal* **2017**, *23* (36), 8623–8627. <https://doi.org/10.1002/chem.201702072>.
- (12) Mann, S. *Biomineralization: Principles and Concepts in Bioinorganic Materials Chemistry*; Oxford University Press, 2001.
- (13) Nudelman, F.; Sommerdijk, N. A. J. M. Biomineralization as an Inspiration for Materials Chemistry. *Angewandte Chemie International Edition* **2012**, *51* (27), 6582–6596. <https://doi.org/10.1002/anie.201106715>.
- (14) Landis, W. J. Mineral Characterization in Calcifying Tissues: Atomic, Molecular and Macromolecular Perspectives. *Connective Tissue Research* **1996**, *34* (4), 239–246. <https://doi.org/10.3109/03008209609005267>.

- (15) Hildebrand. Nanoscale Control of Silica Morphology and Three-Dimensional Structure during Diatom Cell Wall Formation. *Journal of Materials Research* **2006**, *21*, 2689–2698. <https://doi.org/10.1557/jmr.2006.0333>.
- (16) Liu, X.; Theil, E. C. Ferritins: Dynamic Management of Biological Iron and Oxygen Chemistry. *Accounts of Chemical Research* **2005**, *38* (3), 167–175. <https://doi.org/10.1021/ar0302336>.
- (17) Horcajada, P.; Surblé, S.; Serre, C.; Hong, D.-Y.; Seo, Y.-K.; Chang, J.-S.; Grenèche, J.-M.; Margiolaki, I.; Férey, G. Synthesis and Catalytic Properties of MIL-100(Fe), an Iron(III) Carboxylate with Large Pores. *Chemical Communications* **2007**, *0* (27), 2820–2822. <https://doi.org/10.1039/B704325B>.
- (18) Bellido, E.; Guillevic, M.; Hidalgo, T.; Santander-Ortega, M. J.; Serre, C.; Horcajada, P. Understanding the Colloidal Stability of the Mesoporous MIL-100(Fe) Nanoparticles in Physiological Media. *Langmuir* **2014**, *30* (20), 5911–5920. <https://doi.org/10.1021/la5012555>.
- (19) de la Peña Ruigómez, A.; Rodríguez-San-Miguel, D.; Stylianou, K. C.; Cavallini, M.; Gentili, D.; Liscio, F.; Milita, S.; Roscioni, O. M.; Ruiz-González, M. L.; Carbonell, C.; MasPOCH, D.; Mas-Ballesté, R.; Segura, J. L.; Zamora, F. Direct On-Surface Patterning of a Crystalline Lamellar Covalent Organic Framework Synthesized at Room Temperature. *Chemistry – A European Journal* **2015**, *21* (30), 10666–10670. <https://doi.org/10.1002/chem.201501692>.
- (20) Tomašić, V.; Štefanić, I.; Filipović-Vinceković, N. Adsorption, Association and Precipitation in Hexadecyltrimethylammonium Bromide/Sodium Dodecyl Sulfate Mixtures. *Colloid and Polymer Science* **1999**, *277* (2–3), 153–163. <https://doi.org/10.1007/s003960050380>.
- (21) Kume, G.; Gallotti, M.; Nunes, G. Review on Anionic/Cationic Surfactant Mixtures. *J Surfact Deterg* **2008**, *11* (1), 1–11. <https://doi.org/10.1007/s11743-007-1047-1>.
- (22) Dwars, T.; Paetzold, E.; Oehme, G. Reactions in Micellar Systems. *Angewandte Chemie International Edition* **2005**, *44* (44), 7174–7199. <https://doi.org/10.1002/anie.200501365>.
- (23) Kraemer, E. O.; Dexter, S. T. The Light-Scattering Capacity (Tyndall Effect) and Colloidal Behavior of Gelatine Sols and Gels. *J. Phys. Chem.* **1926**, *31* (5), 764–782. <https://doi.org/10.1021/j150275a014>.
- (24) Bail, A. L. Whole Powder Pattern Decomposition Methods and Applications: A Retrospection. *Powder Diffraction* **2005**, *20* (4), 316–326. <https://doi.org/10.1154/1.2135315>.
- (25) Petříček, V.; Dušek, M.; Palatinus, L. Crystallographic Computing System JANA2006: General Features. *Zeitschrift für Kristallographie-Crystalline Materials* **2014**, *229* (5), 345–352.
- (26) Li, W.; Han, Y.-C.; Zhang, J.-L.; Wang, B.-G. Effect of Ethanol on the Aggregation Properties of Cetyltrimethylammonium Bromide Surfactant. *Colloid Journal* **2005**, *67* (2), 159–163. <https://doi.org/10.1007/s10595-005-0075-7>.
- (27) Patterson, A. L. The Scherrer Formula for X-Ray Particle Size Determination. *Phys. Rev.* **1939**, *56* (10), 978–982. <https://doi.org/10.1103/PhysRev.56.978>.
- (28) Pucci, C.; Pérez, L.; Mesa, C. L.; Pons, R. Characterization and Stability of Catanionic Vesicles Formed by Pseudo-Tetraalkyl Surfactant Mixtures. *Soft Matter* **2014**, *10* (48), 9657–9667. <https://doi.org/10.1039/C4SM01575D>.

- (29) Pedersen, J. S. Analysis of Small-Angle Scattering Data from Colloids and Polymer Solutions: Modeling and Least-Squares Fitting. *Advances in Colloid and Interface Science* **1997**, *70*, 171–210. [http://dx.doi.org/10.1016/S0001-8686\(97\)00312-6](http://dx.doi.org/10.1016/S0001-8686(97)00312-6).
- (30) Kandambeth, S.; Dey, K.; Banerjee, R. Covalent Organic Frameworks: Chemistry beyond the Structure. *Journal of the American Chemical Society* **2019**, *141* (5), 1807–1822. <https://doi.org/10.1021/jacs.8b10334>.
- (31) Gao, Q.; Bai, L.; Zhang, X.; Wang, P.; Li, P.; Zeng, Y.; Zou, R.; Zhao, Y. Synthesis of Microporous Nitrogen-Rich Covalent-Organic Framework and Its Application in CO₂ Capture. *Chinese Journal of Chemistry* **2015**, *33* (1), 90–94. <https://doi.org/10.1002/cjoc.201400550>.
- (32) Dong, J.; Wang, Y.; Liu, G.; Cheng, Y.; Zhao, D. Isoreticular Covalent Organic Frameworks for Hydrocarbon Uptake and Separation: The Important Role of Monomer Planarity. *CrystEngComm* **2017**, *19* (33), 4899–4904. <https://doi.org/10.1039/C7CE00344G>.
- (33) Bai, L.; Phua, S. Z. F.; Lim, W. Q.; Jana, A.; Luo, Z.; Tham, H. P.; Zhao, L.; Gao, Q.; Zhao, Y. Nanoscale Covalent Organic Frameworks as Smart Carriers for Drug Delivery. *Chem. Commun.* **2016**, *52* (22), 4128–4131. <https://doi.org/10.1039/C6CC00853D>.
- (34) Horcajada, P.; Chalati, T.; Serre, C.; Gillet, B.; Sebrie, C.; Baati, T.; Eubank, J. F.; Heurtaux, D.; Clayette, P.; Kreuz, C.; Chang, J.-S.; Hwang, Y. K.; Marsaud, V.; Bories, P.-N.; Cynober, L.; Gil, S.; Férey, G.; Couvreur, P.; Gref, R. Porous Metal–Organic-Framework Nanoscale Carriers as a Potential Platform for Drug Delivery and Imaging. *Nature Materials* **2010**, *9* (2), 172–178. <https://doi.org/10.1038/nmat2608>.

Table of Contents